Available online at www.sciencedirect.com
ScienceDirect
Earth and Planetary Science Letters 258 (2007) 465–485
EPSL
www.elsevier.com/locate/epsl

Numerical modeling of crustal block-and-fault dynamics, earthquakes and slip rates in the Tibet-Himalayan region

Alik Ismail-Zadeh [a,b,c,*], Jean-Louis Le Mouël [a], Alexander Soloviev [b,d], Paul Tapponnier [a], Inessa Vorovieva [b]

[a] *Institut de Physique du Globe de Paris, 4 Place Jussieu, Paris 75252, France*
[b] *International Institute of Earthquake Prediction Theory and Mathematical Geophysics, Russian Academy of Sciences, Warshavskoye sh. 79-2, Moscow 117556, Russia*
[c] *Geophysikalisches Institut, Universität Karlsruhe, Hertzstr. 16, Karlsruhe 76187, Germany*
[d] *Earth System Physics, The Abdus Salam International Centre for Theoretical Physics, Miramare, Trieste 34100, Italy*

Received 18 January 2006; received in revised form 24 October 2006; accepted 2 April 2007
Available online 11 April 2007
Editor: C.P. Jaupart

Abstract

The Tibetan plateau and Himalayans have resulted from the continuous Indian and Eurasian plate convergence following their initial collision about 55 million years ago. Earthquakes in the region occur mainly in response to the crustal motion and stress localization associated with this convergence. To understand the basic features of the crustal motion and seismicity in the Tibet-Himalayan region, we develop a numerical model of block-and-fault dynamics. The model structure is composed of six major upper crustal blocks separated by fault planes. These blocks are assumed to be perfectly rigid and move as a consequence of the Indian plate push and of a flow of the lower crust. Deformations take place along the fault planes separating the blocks. The interaction of the blocks along the fault planes is visco-elastic as long as the ratio of the shear stress to the difference between the pore pressure and normal stress remains below a critical strength level. When the critical level is exceeded in some part of a fault plane, an earthquake (stress-drop) occurs causing also failures in adjacent parts of the fault plane. The stress-drop-affected parts of the fault plane enter in a state of creep immediately after the earthquake, and the creep lasts until the stress falls below a certain level. We develop several sets of numerical experiments to analyze the earthquake clustering, frequency-to-magnitude relationships, earthquake focal mechanisms, and fault slip rates in the model. Large events in the numerical experiments cluster on the fault segments associated with the Himalayan Frontal Thrust as well as at some internal faults of the Tibetan plateau. The clustering of earthquakes on a given fault is a consequence of the dynamics of the regional fault system rather than that of the fault only. We show that variations in the relationship of magnitude to frequency of the events are associated with changes in the motion of the upper crustal blocks and depend on the rheological properties of fault plane zones. The focal mechanisms of model events are found to be consistent with that of earthquakes in the region. The synthetic moment rate captures the observed rate of seismic moment release. We demonstrate in the model that the present crustal motion in the region is indeed governed by the north–northeastern movement of India toward Eurasia and the movement of the lower crust. Variations in the rheological properties of

* Corresponding author. Geophysikalisches Institut, Universität Karlsruhe, Hertzstr. 16, Karlsruhe 76187, Germany. Fax: +49 721 71173.
E-mail addresses: aiz@ipgp.jussieu.fr, Alik.Ismail-Zadeh@gpi.uka.de (A. Ismail-Zadeh).

0012-821X/$ - see front matter
doi:10.1016/j.epsl.2007.04.006

fault plane zones and/or in the motion of the lower crust influence rates of the crustal block displacements and slips at the faults separating the blocks. This can explain the discrepancies in estimates of slip rates over short and long time scales at major faults in the region.

Keywords: Tibet; Himalayas; seismicity; numerical modeling; crustal block dynamics; fault slip rate

1. Introduction

Following the closure of the Mesozoic Tethys ocean, the India–Asia collision initiated the development of the Himalayan range and the Tibetan plateau and induced widespread strain in southeastern Asia and China. The Tibetan plateau is underlain by a thick crust (up to 70 to 80 km) as inferred from gravity anomalies and seismic profiles [1–4]. The Himalayan front and the Longmen Shan represent abrupt and steep topographic fronts at the southern and eastern edges of the plateau (Fig. 1). Remarkable features of the Tibetan plateau are its flat topography and predominantly strike-slip faulting [5–13].

There are three distinct views of the active regional deformation which dominate the debate on the mechanics of continental deformation. One view is that the deformation is distributed throughout the continental lithosphere [e.g., 12–14]. Another view is associated with the crustal thinning and the deformation due to a channel flow within the mid-to-lower crust [15–18]. Meanwhile there is growing evidence supporting the alternative view that a substantial part of the deformation of the continents is localized on long and relatively narrow faults and shear zones separating rigid crustal blocks [e.g., 19–22]. Many of these zones cut the base of the crust [23,24], and some extend to the base of the lithosphere [e.g., 25]. Therefore such deformations can be described by motions of crustal blocks separated by faults.

Studies of major Cenozoic fault systems in the Tibet-Himalayan region using various techniques show that a single fault can have various slip rates at different time

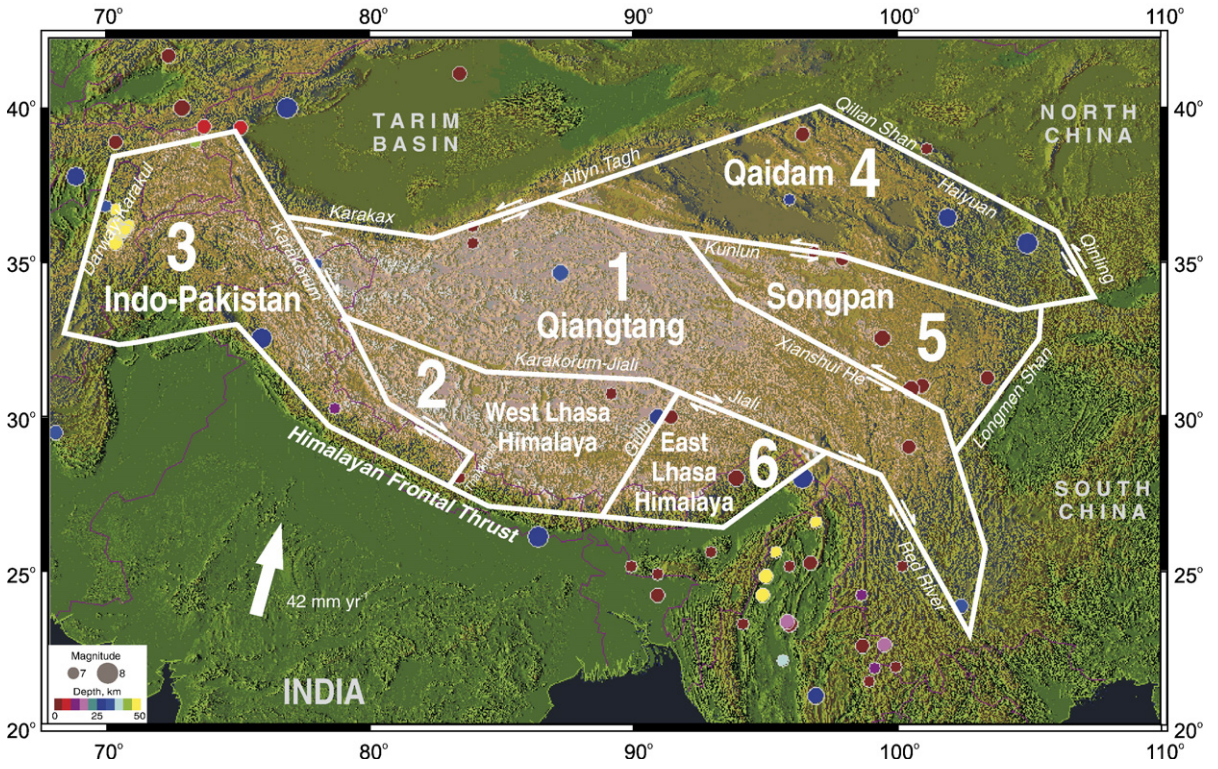

Fig. 1. Topography and observed movements [20] of Tibet and adjacent regions. White bold lines are model faults, and the white arrow indicates the motion of India relative to Eurasia. Earthquake epicenters are marked by circles.

scales when measured by different techniques: satellite radar interferometry (InSAR) [26] and geodetic (GPS) [27–31] for a time scale of a few years; cosmogenic dating for thousands of years [32,33], and geologic measurements for millions of years [9,34–37]. The difference in the slip rate estimates varies up to one order of magnitude, much larger than the uncertainties of each technique.

In this paper we study a *b*lock-*a*nd-*f*ault *d*ynamics model (BAFD model) for the Tibet-Himalayan region in order to answer the following questions: (i) how upper crustal blocks of the Tibetan plateau react to the Indian plate motion and to a flow of the lower crust; (ii) how earthquakes cluster in the system of major regional faults; (iii) how the focal mechanisms of model events are related to the mechanisms of observed earthquakes; and (iv) how rheological properties of the fault zones influence the earthquake clustering and fault slip rates. First we present the basic principles and mathematical statement of the BAFD model (Section 2). The model geometry of the crustal blocks in the Tibetan plateau and model parameters are discussed in Section 3. We present the results of our numerical experiments in Section 4, discuss them in Section 5, and derive then conclusions.

2. Block-and-fault dynamics model

2.1. Basic principles

A model of block-and-fault dynamics is used to analyze how the basic features of seismicity and fault slip rates depend on the crust (lithosphere) structure and dynamics. The basic principles of the model have been developed by Gabrielov et al. [38]. The BAFD model considers a seismic region as a structure of perfectly rigid (upper crustal or lithospheric) blocks divided by infinitely thin fault planes. The blocks interact between themselves and with the underlying medium (lower crust or asthenosphere). The structure of blocks moves in response to prescribed motion of the boundary blocks and of the underlying medium. Because the blocks are perfectly rigid, deformation is localized in the fault zones, and relative block displacements take place along the fault planes. The block motion is defined so that the structure is in a quasistatic equilibrium state.

The interaction of the blocks along the fault planes is visco-elastic (we refer to it as a normal state) as long as the ratio of the shear stress to the difference between the pore pressure and normal stress remains below a certain

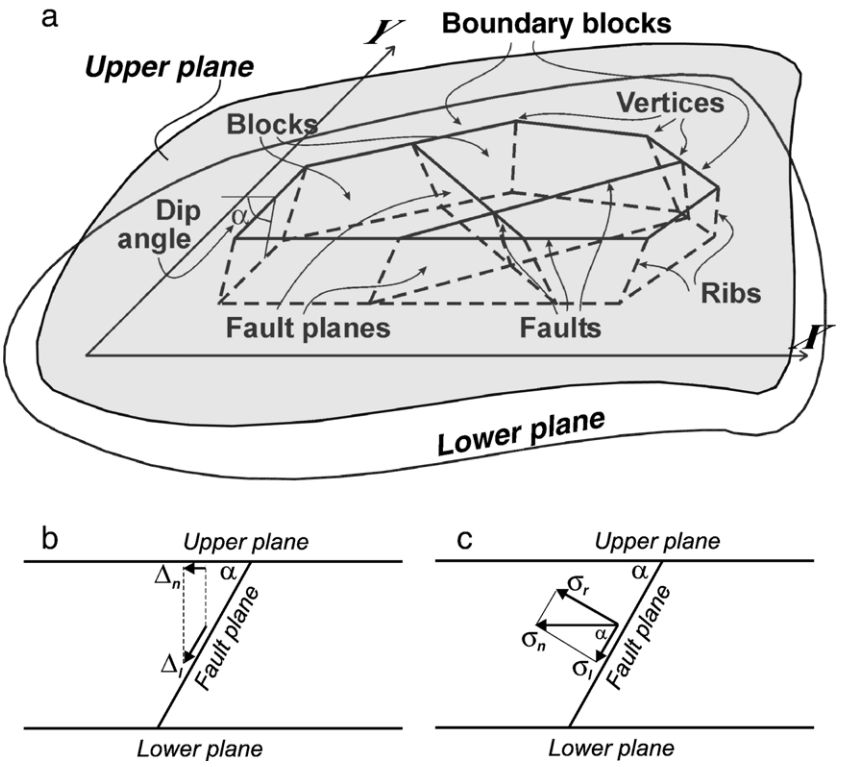

Fig. 2. A sketch of the block-and-fault dynamics model: Model geometry (*a*) and a vertical section of a block-and-fault structure orthogonal to a fault presenting the relative displacements of blocks (*b*) and the forces per unit area (*c*).

strength level. When the critical level is exceeded in some part of a fault plane, a stress-drop (failure) occurs resulting in failures in adjacent parts of the fault planes. The failure produces an earthquake. Immediately after the earthquake the stress-drop-affected parts of the fault planes are in a state of creep. This state differs from the normal state because of a faster growth of inelastic displacements, lasting until the stress falls below a certain level. Thus, the BAFD model generates a catalog of synthetic earthquakes. Using the synthetic catalogs, it is possible to analyze spatial–temporal correlation between earthquakes, their clustering, long-range interaction between the events, and fault slip rates [39]. The model was applied to analyze the lithospheric motion and seismicity in the Vrancea earthquake-prone region of the southeastern Carpathians [40–42], in the Western Alps, and in Sunda Arc [39]. One can determine model parameters for a particular region which fit closely the spatial distribution of seismicity, frequency–magnitude relationship in this region, displacement rates of crustal structures, and fault slip rates.

2.2. Model statement

The block-and-fault structure considered in the model is a bounded and simply connected part of a layer of thickness H limited by two horizontal planes (Fig. 2*a*). The lateral boundaries of the structure and its subdivision into blocks are formed by the portions of planes intersecting the layer; we refer to these planes as *fault planes*. The intersection lines of the fault planes with the upper plane are referred to as *faults*. The fault planes may have arbitrary dip angles, which are specified in the model based on the knowledge of the deep structure of the region under study. A common point of two faults is referred to as a *vertex*. The vertices in the upper and the lower planes are connected by a *rib* of the intersection line of the relevant fault planes (see Fig. 2*a*). The part of a fault plane between two ribs corresponding to successive vertices on the fault is referred to as a *fault segment*. The upper and the lower surfaces of the blocks are polygons. The common part of a block with the lower plane is referred to as a *block bottom*. The block-and-fault structure is bordered by the infinite confining medium. The motion of the confining medium is defined in the area bounded by two ribs of the boundary of the structure (refer to the area as a *boundary block*).

Boundary blocks and the underlying medium are assumed to move due to applied forces. The movements are assumed to be horizontal, their rates are given, and the rate of movement of the underlying medium can vary with the blocks. Dimensionless time is used in the model. All variables depending on time are referred to the unit of the dimensionless time, and the real time corresponding to this unit is estimated when the numerical results are interpreted.

The state of the block-and-fault structure is considered at the discrete time $t_i = t_0 + i\Delta t$ ($i = 1, 2, \ldots$), where t_0 is the initial time. At each time step the translation vectors and the angles of rotation of the blocks are determined in such a way that the structure is in a quasistatic equilibrium. Relative block displacements take place, as assumed, only along fault planes. All displacements are supposed to be infinitely small compared to the block size. Therefore the geometry of the block structure does not change during the simulation and the structure does not move as a whole.

2.3. Interaction of blocks along fault planes and with the underlying medium

Consider a point (X, Y) at the fault plane separating two blocks i and j (for the sake of definiteness, we assume that blocks i and j are on the left and right of the fault, respectively). The components Δx and Δy of the relative displacement of the blocks are defined as follows:

$$\Delta x = x_i - x_j - (Y - Y_c^i)\varphi_i + (Y - Y_c^j)\varphi_j,$$

$$\Delta y = y_i - y_j + (X - X_c^i)\varphi_i - (X - X_c^j)\varphi_j, \qquad (1)$$

where X_c^i, Y_c^i, X_c^j, and Y_c^j are the coordinates of the geometric centers of the block bottoms; (x_i, y_i) and (x_j, y_j) are the translational vectors of the blocks; φ_j and φ_j are the angles of rotation of the blocks about the geometric centers of their bottoms, all depending on time t. A relationship similar to Eq. (1) is used to define the relative displacement of the block and the underlying medium.

We assume that the relative block displacements take place only along fault planes; therefore, the displacement $\Delta = (\Delta_t, \Delta_l)$ along the fault plane is given by

$$\begin{aligned}\Delta_t &= e_x\Delta x + e_y\Delta y, \quad \Delta_l = \Delta_n/\cos\alpha \\ &= (e_x\Delta y - e_y\Delta x)/\cos\alpha \end{aligned} \qquad (2)$$

where Δ_t and Δ_l are the displacement components along the fault plane, parallel and normal to the fault line in the upper plane, respectively; (e_x, e_y) are the direction cosines; α is the dip angle of the fault plane; and Δ_n is the horizontal displacement normal to the fault line in the upper plane (Fig. 2*b*).

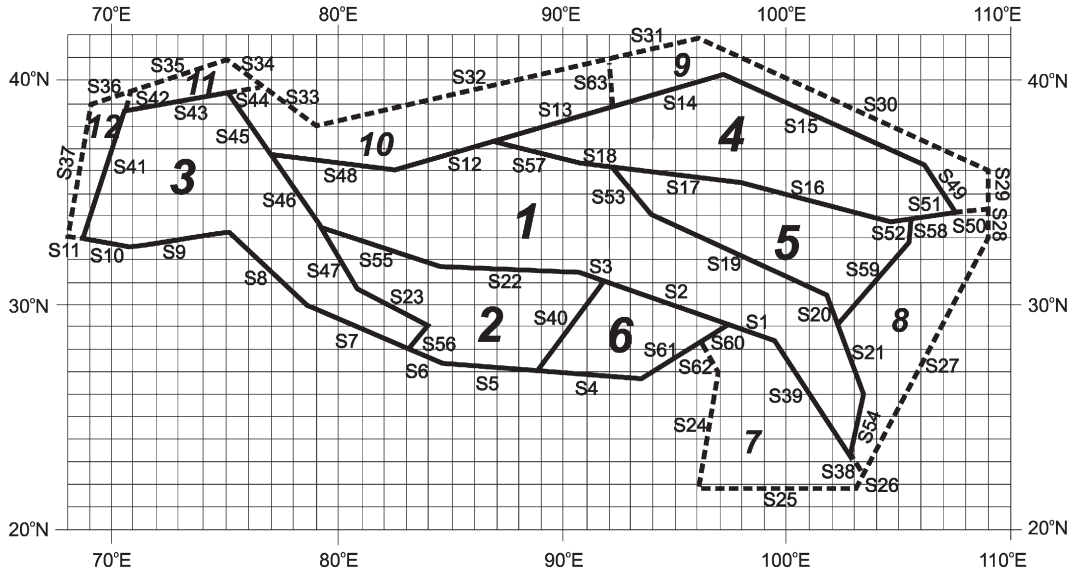

Fig. 3. A block-and-fault structure of the Tibet-Himalayan region. Solid and dashed lines delineate blocks 1 to 6 (structural geological elements) and blocks 7 to 12 (the model boundary elements), respectively. S1–S63 are the fault segments.

Elastic forces arise in the block bases and fault planes in response to the displacement of the blocks relative to the boundary blocks and the underlying medium. At a point (X, Y) the shear stress vector $\sigma=(\sigma_t, \sigma_l)$ (elastic force per unit area acting along the fault plane or the block base) is related to the strain ε at this point by a visco-elastic (Maxwell) rheological law:

$$\left(\frac{\mathrm{d}}{\mathrm{d}t}+\frac{1}{\tau}\right)\sigma=\mu\frac{\mathrm{d}\varepsilon}{\mathrm{d}t} \tag{3}$$

where τ is the relaxation time ($\tau=\eta/\mu$), μ is the shear modulus, and η is the viscosity. For the convenience of subsequent discussions, we present the relationship (3) in the following equivalent form:

$$\sigma=\xi(\Delta-\delta),\quad \frac{\mathrm{d}\delta}{\mathrm{d}t}=\zeta\sigma \tag{4}$$

where $\delta=(\delta_t, \delta_l)$ is the inelastic displacement at a point of the fault planes; $\xi=\mu/a$, $\zeta=a/\eta$, a is the characteristic length ($a=3$ km is assumed in the model); and $\tau=1/(\xi\zeta)$.

In addition to the elastic force, there is a reaction force normal to the fault plane; the work of this force is zero, because all relative movements are tangent to the fault plane. The normal stress (the reaction force per unit area) σ_r is then defined (Fig. 2c)

$$\sigma_r=\sigma_l\ \tan\alpha. \tag{5}$$

The value of σ_r is positive for a tensional stress. Because of the reaction force introduced in the model, there are no vertical forces acting on the blocks and hence no vertical displacement of the blocks. The horizontal movement of the model boundary blocks is prescribed by their translation and rotation about the origin (see Eq. (1)).

The components of the translational vectors of the blocks and the angles of their rotation about the geometric centers of the block bottoms are found from the condition that the total force and the total moment of forces acting on each block must vanish. This is the condition of quasi-static equilibrium of the system and at the same time the condition of minimum energy. The equilibrium equations include only forces caused by specified movements of the underlying medium and of the boundaries of the block-and-fault structure. In fact, it is assumed that the action of all other forces (e.g. gravity) on the structure is ruled out and does not cause displacements of blocks.

The space discretization required to carry out numerical simulations of the BAFD model is made by splitting the surfaces, on which the forces act, into small cells of trapezoidal shape, whose linear size does not exceed a specified parameter χ. The coordinates (X, Y), displacement Δ, inelastic displacement δ, and elastic stress σ are supposed to be the same for all the points of a cell.

2.4. Earthquake and creep

Earthquakes are simulated according to the criterion of the Coulomb failure stress [43] and the dry friction.

Namely, for each cell of the fault plane, we introduce the dimensionless number (proportional to the friction coefficient)

$$\kappa = \frac{|\sigma|}{P - \sigma_r} \tag{6}$$

where $|\sigma|$ is the magnitude of the shear stress along the fault plane, and P is the difference between the lithostatic and pore (hydrostatic) pressure in the fault zone, which is assumed to be equal to 2×10^8 Pa (the typical value at 15 km depth) for all the faults.

Three critical values of κ, $B>H_f>H_s$, are specified for each fault. The initial conditions for the BAFD model – the translation vectors and angles of rotation of the blocks and the inelastic displacements of the cells – are assumed to satisfy the inequality $\kappa<B$ for all cells of the fault planes. If at any time the value of κ exceeds the level B at one or more cells, a failure (earthquake) occurs. An earthquake in the model is defined as an abrupt decrease of the inelastic displacement δ in the cell. The inelastic displacement is updated after the failure:

$$\widetilde{\delta} = \delta + \gamma\sigma \tag{7}$$

where the coefficient γ is determined from the condition that after the failure κ is reduced to the level H_f:

$$\gamma = \frac{1}{\xi}\left(1 - \frac{P}{(|\sigma|/H_f + \sigma_r)}\right). \tag{8}$$

Once the new values of the inelastic displacements for all the failed cells are computed, the translation vectors and the angles of rotation of the blocks are determined to satisfy the condition of the quasi-static equilibrium. If after these computations $\kappa>B$ for some cell(s) of the fault planes, the procedure is repeated for this (these) cell(s); otherwise, the numerical simulation is continued in the ordinary way.

On the same fault plane, the cells in which failure occurs at the same time form a single earthquake. The coordinates of the earthquake hypocenter are defined as the weighted sum of the coordinates of the cells forming the earthquake (the weights are proportional to the areas of the failed cells). The magnitude of the earthquake is estimated using the formula:

$$M = 0.98\log_{10}S + 3.93 \tag{9}$$

where S is the total area of the cells forming the earthquake, measured in km^2 [44].

Immediately after the earthquake, the cells in which the failure occurred are creeping. It means that the parameter ζ_s ($\zeta_s>\zeta$) in Eq. (4) is used instead of ζ for these cells. The cells are in the state of creep as long as $\kappa>H_s$. Once $\kappa\le H_s$, the cells return to the normal state, and henceforth the parameter ζ is used in Eq. (4) for these cells.

3. Block-and-fault structure for the Tibet-Himalayan region

The model structure for the Tibet-Himalayan region is comprised of several crustal blocks delineated by

Table 1
Dip angles of the fault planes in the BAFD model

#	Fault segments	Direction of fault plane slope	Dip angle
1	S1, S2, S3	S–W	85°
2	S4, S5	N	30°
3	S40	E–S	85°
4	S6, S7	N–E	30°
5	S8	N–E	30°
6	S9	N	30°
7	S10, S11	N	30°
8	S41, S42	W–N	85°
9	S43, S44	S–E	40°
10	S45, S46, S47	E–N	85°
11	S48	S	40°
12	S12, S13, S14	S–E	60°
13	S15	S–W	30°
14	S49	N–E	85°
15	S50, S51, S52	S	85°
16	S16	S–W	40°
17	S17, S18	S	40°
18	S53	N–E	85°
19	S19	N–E	85°
20	S20, S21	E–N	85°
21	S54	E	85°
22	S38, S39	S–W	85°
23	S22	S	85°
24	S55	S–W	85°
25	S56	W–N	85°
26	S23	S–W	85°
27	S57	S–W	85°
28	S58	E	85°
29	S59	E–S	85°
30	S60, S61	N–W	30°
31	S62	E–N	85°
32	S24	E–S	85°
33	S25	N	85°
34	S26, S27	W–N	85°
35	S28, S29	W	85°
36	S30	S–W	85°
37	S31, S32	S–E	85°
38	S33, S34	S–W	85°
39	S35, S36	S–E	85°
40	S37	E–S	85°
41	S63	W	85°

Table 2
Displacement rates (V_x, V_y) and angular velocities (ω) of blocks 1–6 predicted by set 1 of numerical experiments

Experiment	Number of synthetic earthquakes and range of their magnitudes	Segments where earthquakes occurred	Block	V_x, mm yr^{-1}	V_y, mm yr^{-1}	ω, 10^{-6} rad yr^{-1}
1.1	86,002	S4–S10, S61	1	1.0418	3.8556	−0.00256
ξ=1.0	$6.19 \le M \le 7.30$		2	13.9496	5.4002	−0.00259
ζ=0.05			3	1.4132	8.1865	−0.00214
			4	1.3327	2.2195	−0.00286
			5	1.2490	1.7154	−0.00260
			6	0.1515	3.8304	−0.00291
1.2	81,775	S4–S10, S61	1	0.5711	2.8969	−0.00176
ξ=5.0	$6.19 \le M \le 8.30$		2	0.1687	4.0696	−0.00179
ζ=0.01			3	0.5784	5.8768	−0.00092
			4	0.8871	1.6063	−0.00203
			5	0.8016	1.3298	−0.00185
			6	−0.0272	3.0110	−0.00216
1.3	54,056	S4–S10, S61	1	0.3344	2.2608	−0.00131
ξ=20.0	$6.19 \le M \le 8.28$		2	0.1608	3.1971	−0.00127
ζ=0.0025			3	0.2122	4.2374	0.00000
			4	0.5730	1.2162	−0.00159
			5	0.5452	1.0424	−0.00141
			6	−0.0065	2.4148	−0.00170
1.4	79,619	S1, S4–S10, S61	1	0.3581	1.7800	−0.00110
ξ=100.0	$6.18 \le M \le 7.65$		2	0.4700	2.5639	−0.00095
ζ=0.0005			3	0.3442	2.9689	0.00066
			4	0.4125	0.9752	−0.00130
			5	0.4325	0.8254	−0.00116
			6	0.2725	1.8943	−0.00144
1.5	91,241	S1, S4–S10, S61	1	0.4155	1.5956	−0.00104
ξ=500.0	$6.18 \le M \le 7.48$		2	0.6713	2.3225	−0.00083
ζ=0.0001			3	0.4993	2.4558	0.00092
			4	0.3639	0.8988	−0.00120
			5	0.4018	0.7492	−0.00108
			6	0.4495	1.6765	−0.00134

Replumaz and Tapponnier [45] on the basis of detailed geomorphic and tectonic field studies and large scale SPOT or LANDSAT imagery analysis [5,7,8,34,46–52]. For the sake of simplicity, we combine several small-size blocks of the Replumaz and Tapponnier model [45] into a single block. The major blocks are separated by thrust and strike-slip faults hundreds of kilometers long. The faults in the model structure do not trace exactly the regional faults, but rather represent the main geometrical features of the faults. The blocks in the model structure are considered as perfectly rigid for time intervals of several thousands years (the model time). Meanwhile, we recognize that blocks bounded by normal or thrust faults stretch or shrink during geological times, but their deformation for the time of several thousand years is insignificant compared to the block sizes.

The Qiangtang platform is the largest Tibetan block (block 1, Fig. 1), which is cut by small normal faults [5,7]. The faults slip at slow rates [53], and hence they are neglected in the model to a first order. Its southern limit follows the dextral Karakorum–Jiali fault zone and is connected eastwards with the Red River fault. The northeast limit of Qiangtang is the Xianshui He fault, which bends southwards into the Xiaojiang fault before abutting the Red River fault. This northern limit follows the Fenguo Shan thrusts [54], between the Xianshui He and the Kunlun faults, then the north branch of the Kunlun fault, to the Altyn Tagh fault. The western limit of the block follows the Karakax and Karakorum faults.

The present limit between India and Asia is the thrust along the Main Himalayan Front separating India from southern Tibet. The central part of South Tibet is rifted into seven small blocks [7]. We divide South Tibet into three main blocks (Fig. 1): West Lhasa Himalayas (block 2), East Lhasa Himalayas (block 6), and Indo-Pakistan (block 3). The Lhasa-Himalayan blocks are limited to the west by the Karakorum fault and to the north by the Karakorum–Jiali fault zone [8,55]. The West Lhasa Himalayas and East Lhasa Himalayas blocks are separated by the Gulu rift zone. The Indo-Pakistan block is bounded to the west by the Darway–Karakul fault, to the north by the Main Pamir Thrust and

to the east by the Karakorum fault. We assume that the southeastern branches of the Karakorum fault terminate into the Thakkhola graben. The Qaidam block (block 4, Fig. 1) is situated between the Kunlun fault to the south, the Altyn Tagh fault to the west and northwest, the Qilian Shan thrust to the north and northeast, and the Qinling fault to the west. And finally, the Songpan block (block 5, Fig. 1) is the triangular wedge between the Kunlun, the Longmen Shan, and the Xianshui He faults.

The six major geological structural elements of the region (blocks 1 to 6) compose the core structure of the BAFD model (Figs. 1 and 3). To avoid the determination of conditions at rigid immobile lateral boundaries of the structure (to the west, north and east of blocks 1 to 6), six additional blocks 7 to 12 are introduced in the model as boundary blocks (Fig. 3). Segments of the boundary blocks S11, S24–S38, S42, S44, S50, S62, and S63 (dashed solid lines) do not correspond to real geological structures, and hence $\xi=0$ is specified for the segments. Therefore, according to Eq. (2), all forces and stress in these fault segments are equal to zero.

Thus, the model structure contains 41 fault planes and 12 blocks in total. The fault planes consist of 63 segments. Dip angles of the fault planes given in Table 1 are estimated from seismic reflections images [e.g. 56,57]; dip angle of 85° is prescribed when either the fault planes are nearly vertical or there is no information on the dip angle. The shallow nature of observed earthquake foci suggests that the upper crust is thin and underlain by a low-viscosity layer [58]. We consider that the average thickness of the rigid crustal blocks is 30 km, and assign $H=30$ km between the upper and lower planes (boundaries) of the model structure.

The following values are prescribed to the parameters of the BAFD model in our numerical experiments: $\xi=1$ (measured in 10^7 Pa m^{-1}) and $\zeta=0.05$ (measured in 10^{-7} m Pa^{-1} yr^{-1}), which correspond to the shear modulus 3×10^{10} Pa and viscosity 2×10^{19} Pa s at the bottom plane of blocks 1–6 ($\tau=20$ yr). For fault segments S1–S10, S12–S23, S39–S41, S43, S45–S49, S51–S61, $\xi=1$ and $\zeta=0.01$, the thresholds for κ are $B=0.1$, $H_f=0.085$, $H_s=0.07$, and $\zeta_s=2$ (measured in 10^{-7} m Pa^{-1} yr^{-1}). The values of the parameters for the time and space discretization are $\Delta t=10^{-3}$ yr and $\chi=16$ km, respectively. The values of the parameters specified here are default values in all numerical experiments (if other values of the parameters are not prescribed).

The numerical simulations were performed for 4000 years starting from zero initial conditions. The total displacements of the blocks are represented by their

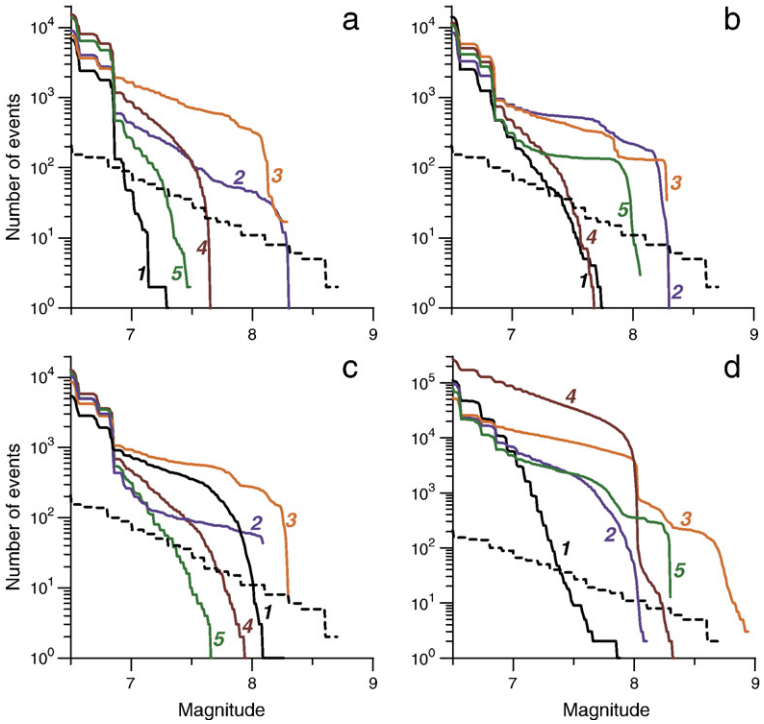

Fig. 4. Cumulated FM plots for synthetic seismicity (solid lines) predicted by numerical experiments: (*a*) set 1 to (*d*) set 4. Index k ($k=1, 2, 3, 4, 5$) at the solid lines presents the number of the experiment in set i ($i=1, 2, 3, 4$). The cumulated FM plot for the observed seismicity from 1967 to 2003 is shown by a dashed line.

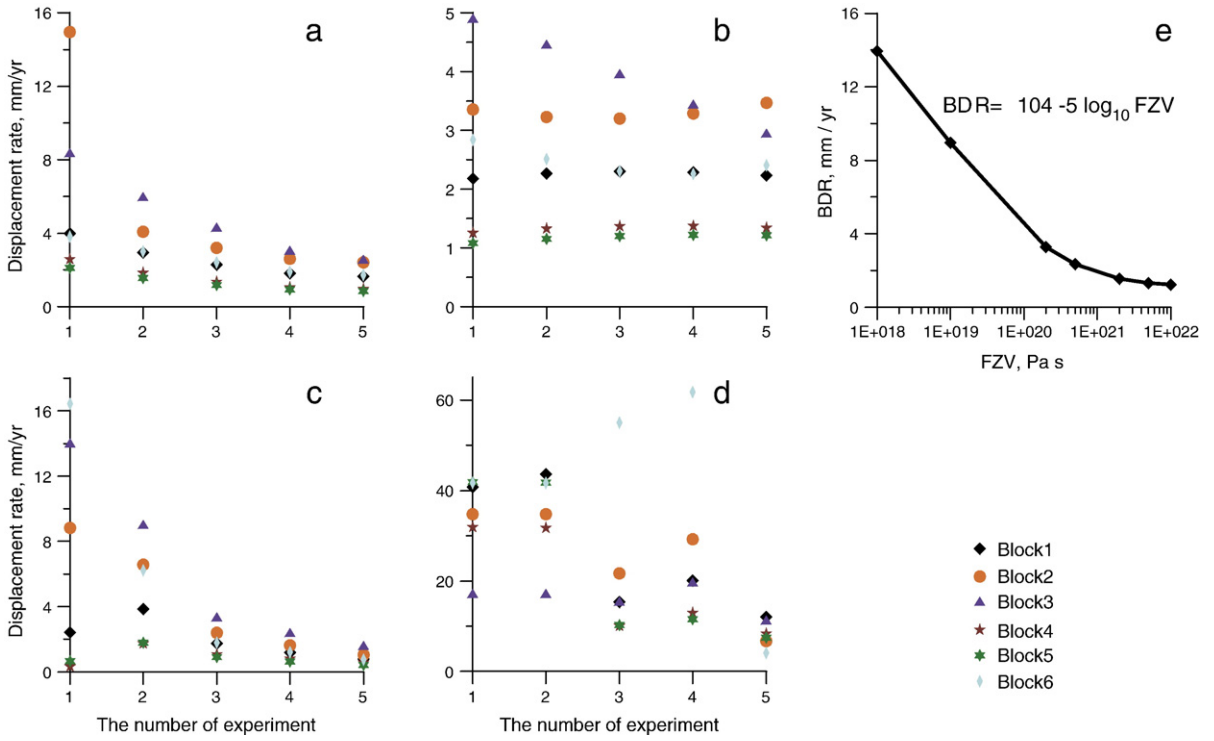

Fig. 5. Displacement rates for each crustal block in the numerical experiments: (*a*) set 1 to (*d*) set 4. Panel (*e*) presents the displacement rate (BDR) of block 3 versus the fault zone viscosity (FZV) for set 3 of the numerical experiments.

translations along the X and Y axes of the reference coordinate system and by the angles of rotation around their geometrical centers. The point with the geographic coordinates 30°N and 90°E is chosen as the origin of the reference coordinate system (Fig. 3). The X axis is the east-oriented parallel passing through the origin of the coordinate system; the Y axis is the north-oriented meridian passing through the origin of the coordinate system.

4. Numerical results

Four sets of numerical experiments have been performed to study the dynamics of the block-and-fault structure in the Tibet-Himalayan region. The experiments analyze how the following factors influence the seismic clustering and the rates of block displacements and fault slips: (1) the resistance of the model boundary (Section 4.1), (2) variations in the movement of the Indian plate with respect to Eurasia (Section 4.2), (3) changes in the elastic and viscous properties of the fault zones (Section 4.3), and (4) variations in the motion of the lower crust (Section 4.4).

In sets 1–3 of the numerical experiments the movement of the boundary formed by segments S4–S10, and S61 is specified (with the rate of U_x=10 mm yr^{-1}, U_y=40 mm yr^{-1}). The rate is constrained by the present rate of convergence between India and Asia [59]. All other parts of the lateral boundary of the structure as well as the medium underlying all the blocks are motionless in sets 1–3. In set 4 the movement of the boundary fault segments as well as the movement of the medium underlying the blocks (lower crust) are specified and constrained by regional GPS data (A. Yin, personal communication).

4.1. Effect of the model boundary resistance

In set 1 of experiments different values of coefficients ξ and ζ for boundary blocks 7–12 are specified (see Table 2). The increase in the shear modulus and viscosity of the lower crust (precisely, at the interface between the model blocks and the underlying medium) from experiment 1.1 to 1.5 results in a stronger resistance of blocks 7–12 with respect to the movements of blocks 1–6.

Blocks 1, 2, and 4–6 rotate clockwise, and block 3 rotates clockwise in experiments 1.1 and 1.2 and counterclockwise in experiments 1.4 and 1.5 (Table 2). When the GPS data are viewed in a fixed Eurasian frame

Table 3
Displacement rates (V_x, V_y) and angular velocities (ω) of blocks 1–6 predicted by set 2 of numerical experiments

Experiment, U_x, U_y, mm yr^{-1}	Number of synthetic earthquakes and range of their magnitudes	Segments where earthquakes occurred	Block	V_x, mm yr^{-1}	V_y, mm yr^{-1}	ω, 10^{-6} rad yr^{-1}
2.1	83,018	S4–S10, S61	1	0.1118	2.1802	−0.00117
U_x=0	$6.19 \le M \le 7.75$		2	−0.9283	3.2229	−0.00150
U_y=40			3	−0.4491	4.8629	−0.00095
			4	0.5053	1.1452	−0.00129
			5	0.4178	1.0006	−0.00260
			6	−0.9748	2.6717	−0.00185
2.2	59,260	S4–S10, S61	1	0.2730	2.2505	−0.00128
U_x=6.946	$6.19 \le M \le 8.30$		2	−0.1488	3.2226	−0.00135
U_y=39.392			3	0.0252	4.4397	−0.00027
			4	0.5570	1.2028	−0.00156
			5	0.5119	1.0363	−0.00138
			6	−0.2832	2.5015	−0.00176
2.3	58,978	S4–S10, S61	1	0.4243	2.2632	−0.00135
U_x=13.681	$6.19 \le M \le 8.28$		2	0.6248	3.1403	−0.00116
U_y=37.588			3	0.4906	3.9102	0.00041
			4	0.5936	1.2293	−0.00162
			5	0.5917	1.0456	−0.00144
			6	0.4093	2.2705	−0.00162
2.4	82,495	S4–S10, S61	1	0.5648	2.2202	−0.00139
U_x=20.0	$6.19 \le M \le 7.68$		2	1.3842	2.9806	−0.00094
U_y=34.641			3	0.9418	3.2880	0.00107
			4	0.6156	1.2255	−0.00164
			5	0.6567	1.0293	−0.00146
			6	1.0941	1.9829	−0.00144
2.5	79,412	S4–S10, S61	1	0.6929	2.1210	−0.00140
U_x=25.712	$6.19 \le M \le 8.06$		2	2.1178	2.7446	−0.00069
U_y=30.642			3	1.3724	2.5832	0.00171
			4	0.6225	1.1908	−0.00161
			5	0.7059	0.9866	−0.00145
			6	1.7603	1.6411	−0.00124

of reference [28,29,60–62], the central and eastern parts of the region (corresponding to blocks 1, 2, 4–6 in the BAFD model) move east–southeast and the western part of the region (corresponding to block 3) tends to move north–northwest relative to Siberia. These observations are consistent with the model predictions on the displacement rates of the crustal blocks.

Synthetic earthquakes occur on segments S4–S10, and S61 in all experiments and also on segment S1 in experiments 1.4 and 1.5. The plots of the cumulative number of earthquakes with magnitudes greater that M as a function of magnitude M (thereinafter we refer to as *FM plots*) for synthetic seismicity obtained in set 1 of experiments are presented in Fig. 4*a*. The seismicity generated by the model experiments is associated with the fault system of the Himalayan Frontal Thrust, where the highest level of seismic activity is observed. The FM plot for the observed seismicity is also shown in Fig. 4*a* (dashed line). Note that the FM plots for synthetic events are shifted upwards due to the larger number of the events compared to the number of seismic events in the region. Comparing the slopes of the FM plots for the observed and synthetic seismicity, we see that the results of experiment 1.3 give the closest fit to the observed slope. The values of the model parameters specified in experiment 1.3 are used in all other sets of numerical experiments.

The displacement rates of the blocks and slip rates at the faults, separating the blocks, decrease with the increase of the shear modulus and viscosity of the lower crust. In experiment 1.1 the maximum displacement rates of the Indo-Pakistan and West Lhasa Himalayas blocks separated by the Karakorum fault are about 15 mm yr^{-1} and 8 mm yr^{-1}, respectively (Fig. 5*a*). These rates drop to about 3 mm yr^{-1} in experiment 1.5 and to even lesser values (about 1 mm yr^{-1}) for other blocks.

4.2. Effect of the Indian plate movement

In set 2 of experiments we analyze how the direction of the Indian plate motion with respect to Eurasia influences

Table 4
Displacement rates (V_x, V_y) and angular velocities (ω) of blocks 1–6 predicted by set 3 of numerical experiments

Experiment	Number of synthetic earthquakes and range of their magnitudes	Segments where earthquakes occurred	Block	V_x, mm yr^{-1}	V_y, mm yr^{-1}	ω, 10^{-6} rad yr^{-1}
3.1	30,815	S4–S10, S61	1	0.8293	2.2719	−0.00110
ξ=0.01	$6.19 \le M \le 8.26$		2	2.3584	8.5152	−0.00078
ζ=1.0			3	2.1784	13.7672	0.00720
ζ_s=200.0			4	0.1035	0.3071	−0.00081
			5	0.3752	0.5364	−0.00099
			6	3.2372	16.1060	−0.00068
3.2	64,098	S4–S10, S61	1	1.1591	3.6741	−0.00248
ξ=0.1	$6.19 \le M \le 8.09$		2	1.6342	6.3730	−0.00219
ζ=0.1			3	1.1149	8.8900	0.00212
ζ_s=20.0			4	0.6082	1.6282	−0.00262
			5	0.9460	1.5158	−0.00253
			6	1.4411	6.0640	−0.00446
3.3	61,907	S4–S10, S61	1	0.2168	1.7204	−0.00098
ξ=2.0	$6.19 \le M \le 8.30$		2	−0.0252	2.3880	−0.00099
ζ=0.005			3	0.1492	3.2753	−0.00033
ζ_s=1.0			4	0.4972	0.9493	−0.00116
			5	0.3966	0.8089	−0.00105
			6	−0.1422	1.7843	−0.00121
3.4	94,701	S1, S4–S10, S61	1	0.1499	1.1937	−0.00069
ξ=5.0	$6.18 \le M \le 7.95$		2	−0.0726	1.6318	−0.00072
ζ=0.002			3	0.1561	2.3282	−0.00047
ζ_s=0.4			4	0.4108	0.6887	−0.00077
			5	0.2610	0.5772	−0.00072
			6	−0.1521	1.1974	−0.00080
3.5	105,478	S1, S4–S10, S46, S61	1	0.1137	0.7844	−0.00047
ξ=20.0	$6.18 \le M \le 7.67$		2	−0.0281	1.0517	−0.00048
ζ=0.0005			3	0.1808	1.5307	−0.00043
ζ_s=0.1			4	0.3122	0.4844	−0.00049
			5	0.1628	0.3940	−0.00048
			6	−0.0866	0.7479	−0.00050
3.6	110,120	S1, S4–S10, S56, S61	1	0.1018	0.6754	−0.00040
ξ=50.0	$6.10 \le M \le 7.52$		2	−0.0101	0.8966	−0.00041
ζ=0.0002			3	0.1821	1.3034	−0.00039
ζ_s=0.04			4	0.2788	0.4292	−0.00041
			5	0.1361	0.3455	−0.00041
			6	−0.0635	0.6301	−0.00042
3.7	109,808	S1, S4–S10, S56, S61	1	0.0963	0.6359	−0.00038
ξ=100.0	$6.10 \le M \le 7.33$		2	−0.0039	0.8399	−0.00038
ζ=0.0001			3	0.1807	1.2184	−0.00038
ζ_s=0.02			4	0.2666	0.4090	−0.00038
			5	0.1258	0.3282	−0.00038
			6	−0.0554	0.5876	−0.00039

the seismicity and displacement rates of blocks 1 to 6. The direction of the motion is varied from north to northeast; the angle of the velocity with the meridian increases from 0° to 40° (every 10°) from experiment 2.1 to 2.5. The velocity (U_x, U_y) of the motion (in mm yr^{-1}) are prescribed at segments S4–S10, and S61 (Table 3). In all experiments of set 2, blocks 1, 2, 4, 5, and 6 rotate clockwise, block 3 rotates clockwise in experiments 2.1 and 2.2 and counterclockwise in other experiments; synthetic earthquakes occur on segments S4–S10, and S61. Cumulated FM plots for the synthetic seismicity obtained in this set of experiments as well as that for the observed seismicity are presented in Fig. 4*b*. The slope of the FM plot for synthetic seismicity generated in experiment 2.3 is the closest to the slope of the FM plot for the observed earthquakes. The numerical experiments show that the change in the direction of the Indian plate motion affects mainly the displacement rates of the Indo-Pakistan block (Fig. 5*b*). The rates of the displacement of other blocks vary slightly.

Table 5
Translational velocity (w_x, w_y), in mm yr^{-1}, and angular (ω) velocity, in rad yr^{-1}, prescribed to the bottoms of blocks 1–6 in set 4 of numerical experiments

Block no.	Experiment 4.1			Experiment 4.2		
	w_x	w_y	ω	w_x	w_y	ω
1	20.0	20.0	0.0	20.0	20.0	0.0
2	10.0	30.0	0.0	10.0	30.0	0.0
3	−10.0	30.0	0.0	−10.0	30.0	0.0
4	20.0	10.0	0.0	20.0	10.0	0.0
5	10.0	0.5	0.0	30.0	00.0	0.0
6	20.0	30.0	0.0	20.0	30.0	0.0

Block no.	Experiment 4.3			Experiment 4.4			Experiment 4.5		
	w_x	w_y	ω	w_x	w_y	ω	w_x	w_y	ω
1	12.4	−29.3	0.002	12.4	−29.3	0.0	40.0	−10.0	0.0
2	29.4	198.1	−0.148	29.4	198.1	0.0	0.0	0.0	0.0
3	−66.0	11.9	−0.156	−66.0	11.9	0.0	0.0	0.0	0.0
4	7.7	−3.2	0.120	7.7	−3.2	0.0	40.0	5.0	0.0
5	47.8	−17.8	0.181	47.8	−17.8	0.0	50.0	0.0	0.0
6	185.2	73.9	1.229	185.2	73.9	0.0	0.0	0.0	0.0

4.3. Influence of the elastic properties and viscosity of fault zones

In set 3 of experiments, the values of the coefficients ξ, ζ, and ζ_s at internal fault segments S1–S3, S12–S23, S39–S41, S43, S45–S49, and S51–S60 are varied (Table 4), i.e., the shear modulus and viscosity of the relevant fault zones increase from experiment 3.1 to 3.7. In all experiments of this set, blocks 1,2,4–6 rotate clockwise, block 3 rotates counterclockwise in experiments 3.1 and 3.2 and clockwise in other experiments (Table 4). Synthetic earthquakes occur on segments S4–S10, S61, S46, and S56. Cumulated FM plots for synthetic seismicity obtained in set 3 of the experiments are presented in Fig. 4*c*. The slopes of the FM plots for these experiments (except experiments 3.2 and 3.3) differ essentially from the slope of the FM plot for the observed seismicity. From experiments 3.3 to 3.7 the number of large events decreases as the resistance to slip of fault planes increases (with the shear modulus and viscosity). In experiment 3.1 the maximum displacement rates of the Indo-Pakistan and Lhasa Himalayas (blocks 3, 2, and 6) are about 14, 9, and 16 mm yr^{-1}, respectively (Fig. 5*c*). The rates decrease to about 1 mm yr^{-1} at these blocks in experiment 3.7 and to even lesser values (ca. 0.3 mm yr^{-1}) for the other model blocks. Fig. 5*e* presents the displacement rate of the Indo-Pakistan block versus the fault zone viscosity.

4.4. Effect of a lower crustal flow

In set 4 of experiments we analyze the influence of a lower crustal flow on seismicity and rates of block displacements and fault slips. Velocities of the underlying medium (lower crust) are prescribed to the bottom of blocks 1 to 6 (see Table 5), and movement of the boundary fault segments is specified for each numerical experiment (see Table 6). The velocities of the underlying medium and of the boundary fault segments are chosen such a way to keep the block movements close to the regional observed movements. Values ζ_s=200, 0.4, 0.4, 0.1, and 0.5 are assigned to all fault segments of blocks 1 to 6 in experiment 4.1, 4.2, 4.3, 4.4, and 4.5 respectively.

In experiments 4.1 and 4.2, blocks 4 and 5 rotate clockwise and blocks 1–3 and 6 counterclockwise. In experiments 4.3–4.5, blocks 1, 2, 4–6 rotate clockwise, block 3 rotates clockwise in experiments 4.3 and 4.5, and counterclockwise in experiment 4.4. Synthetic seismicity occurs on many segments of the block-and-fault structure (see Table 7). Cumulated FM plots for

Table 6
Velocities (w_x, w_y), in mm yr^{-1}, prescribed to the boundary faults segments in set 4 of numerical experiments

Boundary fault segments	Experiments 4.1 and 4.2		Experiments 4.3–4.5	
	w_x	w_y	w_x	w_y
S4–S10	20.0	20.0	14.0	42.0
S41	20.0	−10.0	10.0	28.6
S43, S45, S48, S12	10.0	0.0	−0.4	13.8
S13, S1	0.0	10.0	2.6	3.4
S15	0.0	10.0	3.0	−0.6
S49, S51, S58, S59, S21, S54	0.0	10.0	4.9	−3.3
S1, S39	20.0	60.0	4.0	−14.4
S60, S61	0.0	0.0	4.4	−2.1

Table 7
Displacement rates (V_x, V_y) and angular velocities (ω) of blocks 1–6 predicted by set 4 of numerical experiments

Experiment	Number of synthetic earthquakes and range of their magnitudes	Segments where earthquakes occurred	Block	V_x, mm yr^{-1}	V_y, mm yr^{-1}	ω, 10^{-6} rad yr^{-1}
4.1	453,590	S2, S4, S8–S10, S12–S17, S19, S22,	1	1.9398	43.7267	0.00949
	$6.11 \le M \le 7.88$	S23, S40, S45, S47, S48, S51, S53,	2	23.8765	25.2575	0.02377
		S55, S57, S59–S61	3	16.8656	−1.6185	0.01658
			4	−0.6103	31.9298	−0.01236
			5	11.3545	40.3355	−0.00747
			6	23.4176	34.4941	0.02046
4.2	272,134	S2, S4, S8–S10, S12–S17, S19, S22,	1	1.9966	43.5533	0.00952
	$6.11 \le M \le 8.10$	S23, S40, S45, S47, S48, S51, S53,	2	23.8396	25.3284	0.02354
		S55, S57, S59–S61	3	16.8578	−1.5547	0.01673
			4	−0.4964	31.7046	−0.01226
			5	11.4195	40.1542	−0.0074
			6	23.4154	34.5107	0.02015
4.3	146,042	S1, S2, S4–S10, S19–21, S23, S39,	1	10.0807	11.556	−0.01166
	$6.18 \le M \le 8.94$	S40, S46–S48, S51, S54, S59–S61	2	7.3091	20.4192	−0.01043
			3	0.3019	15.1812	−0.00083
			4	8.1416	5.9532	−0.01048
			5	9.726	3.2768	−0.00882
			6	54.5164	−7.3917	−0.00275
4.4	706,344	S1, S2, S4, S5, S7–S10, S12, S13,	1	11.7401	16.3832	−0.01635
	$6.03 \le M \le 8.33$	S21, S23, S39–S41, S45–S49, S52,	2	10.6794	27.1760	−0.01272
		S54, S59–S61	3	1.5833	19.4127	0.01430
			4	9.6440	8.6736	−0.01637
			5	10.4403	4.8456	−0.01552
			6	61.6614	−3.7210	−0.02689
4.5	317,835	S1, S3–S10, S12–14, S19, S21, S23,	1	12.0332	−0.9252	−0.00911
	$6.10 \le M \le 8.30$	S39, S41, S46–S48, S54–S57, S59	2	4.4600	4.9507	−0.01058
			3	1.4647	10.9194	−0.00038
			4	8.3325	0.1872	−0.00504
			5	7.4692	−0.2398	−0.00633
			6	4.0598	−0.2314	−0.01009

seismic events (predicted by these experiments and observed) are presented in Fig. 4*d*. The slopes of the plots for experiments 4.3–4.5 are rather close to the slope of the plot for the observed seismicity. The numerical experiments show that displacement rates of the crustal blocks vary with the velocities of the underlying medium and boundary segments (Fig. 5*d*).

5. Discussion

Numerical models of crustal dynamics provide a quantitative insight into earthquake preparation process and movements in the crust. A sequence of earthquakes is generated by a fault network rather than each earthquake by a segment of a single fault. Moreover, statistical and phenomenological studies of seismicity based on observed earthquake catalogs have the disadvantage that the reliable data cover a time interval of less than 100 years, rather short compared to the duration of tectonic processes responsible for seismic activity. A reasonable approach is to study the crustal motion and associated seismicity by numerical modeling and to analyze the synthetic earthquakes and slip rates so obtained [e.g., 39,63].

5.1. Earthquakes

When only the movement of the Indian plate is specified as a driving force in the BAFD model (sets 1 to 3 of numerical experiments), large (M>6.5) synthetic events are clustered mainly on the fault segments associated with the Himalayan Frontal Thrust (Fig. 6b). This movement alone fails to transmit enough stress to the northern and north-eastern parts of the Tibetan plateau to produce in the model the earthquakes observed in the region. An introduction of the movement of the lower crust along with the Indian plate movement, results in earthquakes on the internal fault segments, e.g., on segments of Altyn Tagh, Karakorum, and Kunlun faults, and the Gulu rift zone (Fig. 6c–f). Hypocenters of the modeled events are located mainly at depths ranging from 10 to 20 km.

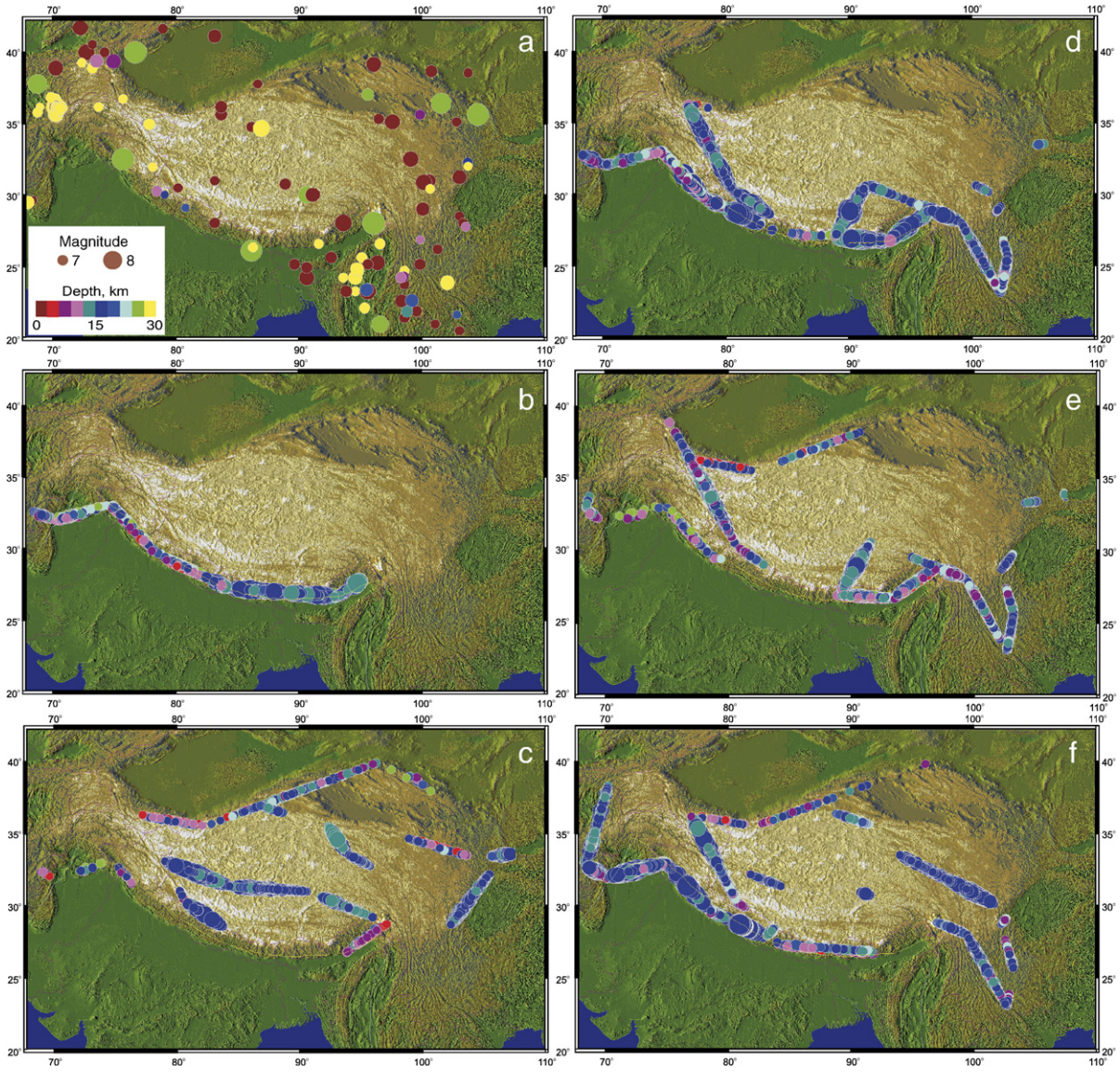

Fig. 6. Spatial distribution of large (M>6.5) earthquakes in the Tibet-Himalayan region. (a) Observed seismicity since 1900. (b–f) Synthetic seismicity in experiments 3.7 (b), 4.2 (c), 4.3 (d), 4.4 (e), and 4.5 (f).

Table 8 presents maximum magnitudes of synthetic events on fault segments for three numerical experiments. The largest events (M=8.9) in the model were obtained in experiment 4.3. They occurred on segment 40, which is associated with the Gulu rift zone. It is remarkable to mention that the frequency of occurrence of these largest events varies considerably: the second of the five events occurred 1204 model years after the first event, the new event in 252 years after the second one, and the last two events with the time interval of 48 and 144 years, respectively, after the third event. The maximum magnitude (M=8.3) of the modeled events in Himalayas (segments 4–10, 60, 61) is lower than that of observed events in the region. In fact, the maximum magnitude (as well as clustering) of synthetic events depends on the block structure geometry, the prescribed motion and the other parameters of the model. It depends also on the choice of Eq. (9) used to define the magnitude of the synthetic events. Wells and Coppersmith [64] updated the relationship between magnitude and rupture area and estimated the absolute term in Eq. (9) to be 4.07. Hence, if the updated relationship is employed in the model, earthquake magnitudes could be slightly higher. The slope of the FM plots provides more

Table 8
Maximum magnitude (M_{max}) and slip angle (β) of modeled earthquakes at fault segments

Fault segment	Numerical experiments					
	4.3		4.4		4.5	
	M_{max}	β	M_{max}	β	M_{max}	β
1	7.25	−90	7.65	−90	7.1	−100
2	7.25	−75	6.8	−5	–	–
3	–	–	–	–	7.3	110
4	8.2	130	7.35	−105, 140	6.9	80
5	6.9	80	6.5	80	7.05	80
6	6.8	100	–	–	6.8	100
7	8.25	90	6.55	−100, 105	8.3	100
8	8.25	120	6.7	120	8.3	120
9	7.5	60	6.8	65	8.25	60
10	7.8	90	6.9	100	7.85	100
12	–	–	6.7	30	6.8	−70
13	–	–	6.6	70	6.6	−60
14	–	–	6.6	70	6.6	−60
19	7.0	−90	–	–	8.0	−90
20	6.5	−90	–	–	–	–
21	7.0	−100	–	–	7.0	−70
23	8.0	−100	7.05	−90	6.9	−120
39	7.35	−85	6.55	−100, 105	7.25	−90
40	8.9	−90	8.3	−90	–	–
41	–	–	6.9	−135	7.7	−175
45	–	–	7.0	−100	–	–
46	7.85	−90	7.7	−90	7.85	−100
47	7.85	−90	7.6	−90	7.4	−100
48	6.8	60	6.9	70	7.25	−90
49	–	–	6.7	−90	–	–
51	6.9	−100	–	–	–	–
52	–	–	6.8	−60	–	–
54	7.3	−100	7.05	−90	6.7	−60
55	–	–	–	–	7.05	−135
56	–	–	–	–	7.05	−100
57	–	–	–	–	7.05	−60
59	6.85	−110	7.05	−100	6.9	−100
60	8.2	140	7.2	−105, 135	–	–
61	8.2	140	7.2	−105, 135	–	–

essential information on earthquake magnitudes. In some experiments the slope of the FM plots for the synthetic events is rather close to that for observed seismicity in the magnitude range from 6.8 to 8.2. The shift in the frequency of occurrence of small synthetic events ($M<6.8$) depends on the discretization of fault segments in the model. The present linear size of the cells composing fault segments is 16 km, and the minimum magnitude of synthetic events ($M\sim6$) is constrained by this size. If smaller cell size (e.g., 3 km) is introduced in the model, the number of events with $M\sim6$ reduces, because a part of stress drops on smaller cells, resulting in earthquakes of smaller magnitudes (Fig. 7).

The numerical results demonstrate that the slope of the FM plots and clustering of large earthquakes are sensitive to the changes in the movements of the lower crust and in the rheological properties of fault plane zones in the Tibetan plateau. Large events localize only on some of the faults, but not on all of the individual faults where the elastic and viscous coefficients were equally changed. This illustrates the fact that the BAFD model does describe the dynamics of a network of crustal blocks and faults rather than the dynamics of individual fault planes.

We have also analyzed the focal mechanisms of the synthetic earthquakes and computed the angle β between the slip direction (in the fault plane) and the fault line. Left- and right-lateral strike-slip (SS) takes place for $\beta=0$ and $\pm180°$, respectively; normal (NF) and thrust (TF) faulting occur for $\beta=90°$ and $\beta=-90°$, respectively. Table 8 shows slip angles at fault segments for three experiments. The value of a slip angle on a fault segment is determined as the value of the angle corresponding to the maximum in the distribution of all slip angles at the fault segment. In a few cases the distribution shows two distinct maximums (see Table 8), which can be associated with a relatively large block rotation resulting in tension at one end of the fault segment and in compression at its other end. Fig. 8 illustrates the stress regimes for the Tibet-Himalayan region defined mainly from the determination of fault plane solutions for the regional earthquakes. A comparison of the modeled and observed data shows a reasonably good agreement between the focal mechanisms of the synthetic and observed earthquakes. Namely, in both cases (in the model and reality) most thrust

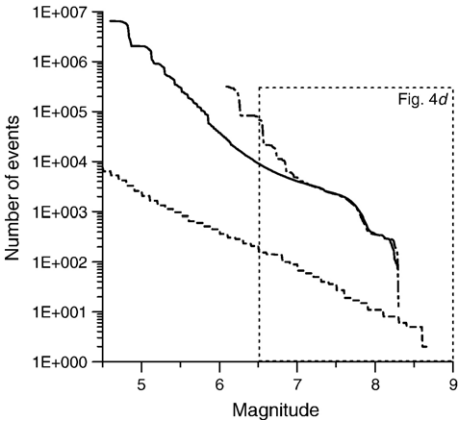

Fig. 7. Cumulated FM plots for synthetic seismicity predicted by numerical experiments with two different cell sizes: 16 km (experiment 4.5, dot-dashed line) and 3 km (solid line). The dashed line presents the cumulated FM plot for the observed regional seismicity. The dotted rectangular illustrates the domain of Fig. 4*d*.

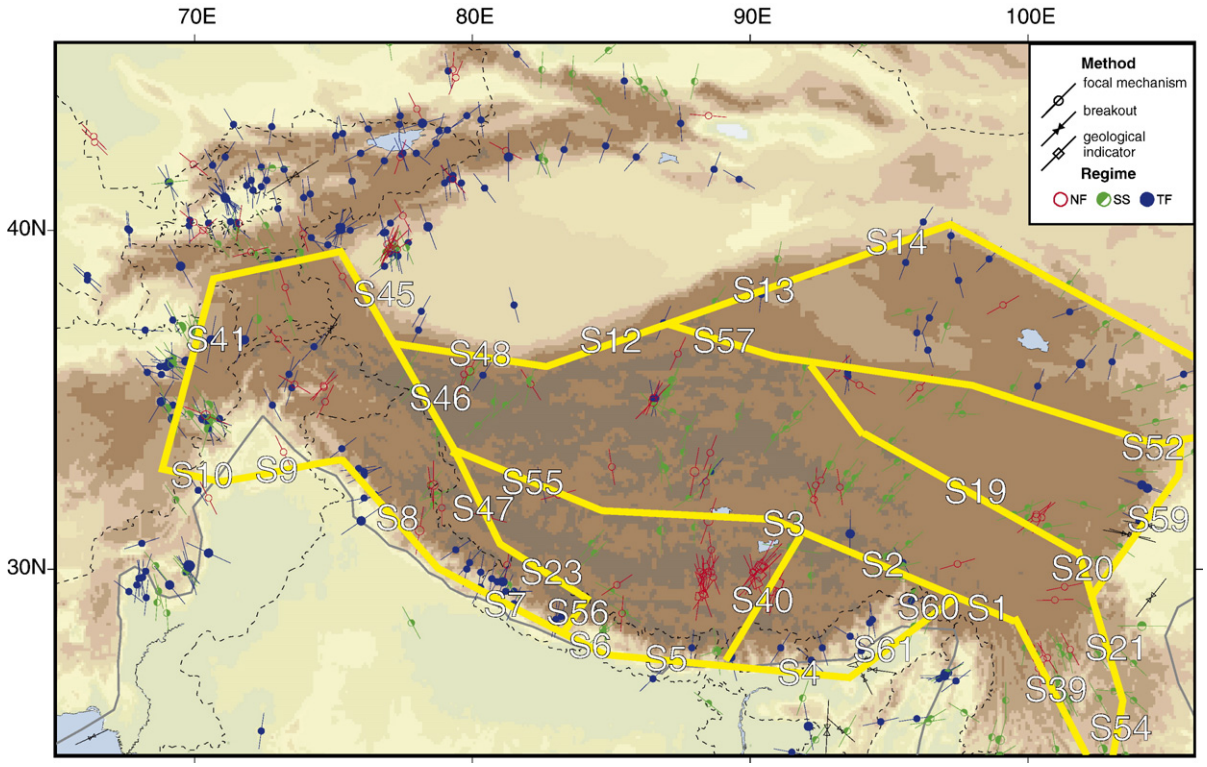

Fig. 8. Regional stress regimes derived mainly from focal mechanisms of earthquakes (compiled from on-line data of World Stress Map, release 2004, http://www.world-stress-map.org). Yellow lines present the model block structure and fault segments.

faulting events occur on the Himalayan seismic belt and normal faulting events on the Gulu rift.

We analyze the rate of seismic moment release for the observed and synthetic events. The observed seismic moment rate for shallow events in the Tibet-Himalayan region (in the depth range from 0 to 30 km corresponding to the model depth range and covering the area of 20 to 42°N and 68 to 110°E) has been estimated by using a catalogue of earthquakes recorded from 1902 to 2000 and the following relation between the seismic moment M_0 and the magnitude M: $\log M_0 = 16.1 + 1.5M$. The observed moment rate is found to be about 0.50×10^{21} N m yr^{-1} for the region. Moment rates are also calculated for synthetic events (e.g., $M_0 = 0.12 \times 10^{21}$ N m yr^{-1} for experiment 3.3; 0.97×10^{20} N m yr^{-1} for experiment 3.7; 0.56×10^{22} N m yr^{-1} for experiment 4.3; 0.81×10^{22} N m yr^{-1} for experiment 4.4; and 0.94×10^{21} N m yr^{-1} for experiment 4.5). The higher seismic moment rates in experiments 4.3 and 4.4 (as compared to the observed rates) are associated with the large magnitude of synthetic events and with the large number of the events obtained in the respective experiments. On the other hand, 100 years is likely to be insufficient time to record a complete cycle of seismic energy release in the Tibet-Himalayan region.

5.2. Block and fault slip rates

The results of the numerical experiments based on the BAFD model allow us to interpret the contemporary movements in the Tibet-Himalayan region as motions of rigid upper crustal blocks driven by the north–northeastward indentation of India into Eurasia and a lower crustal flow. The experiments of sets 1 and 3 show that the weaker is the resistance of the lower crust and fault zones, the larger are the displacement rates of the upper crustal blocks and the relative slip rates at the faults separating the blocks. Moreover if the motion of the lower crust is introduced in the model as prescribed movements of the block bottoms (set 4 of numerical experiments), fault slip rates increase significantly. The average displacement rates of the crustal blocks and fault slips vary from 0.01 to 60 mm yr^{-1} in different experiments (Fig. 5 and Table 9). Note that the numerical simulations are made for 4000 years in all experiments, and hence our results should explain fault slip and block displacements rates derived from GPS measurements, rather than from geological observations. Measurements of slip rates on some faults of the Tibet-Himalayan region using different techniques show that the faults may slip at different rates for different time scales. Estimates of the Holocene slip

Table 9
Slip rates (in mm yr^{-1}) at fault segments predicted by numerical experiments

Segment's number	Numerical experiment								
	1.1	3.1	3.6	3.7	4.1	4.2	4.3	4.4	4.5
2	0.724000	0.020475	0.245406	1.410206	23.383301	23.254008	48.31069	54.57422	7.96045
3	1.342881	0.030456	0.275675	0.645170	28.681746	28.454760	9.304289	10.845051	9.529707
12	1.335271	0.031420	0.363151	0.235935	43.775439	43.604750	15.335541	19.969854	12.020324
13	1.960653	0.033695	0.150877	0.028792	31.958756	31.730860	10.086208	12.791950	8.388929
14	0.839146	0.020712	0.172250	0.031696	31.958751	31.730855	10.086207	12.791947	8.388930
16	0.413789	0.017477	0.035915	0.034995	14.635503	14.619764	3.114263	3.889988	1.069105
17	0.413789	0.017477	0.035915	0.034995	14.635499	14.619760	3.114263	3.889988	1.069104
18	1.347416	0.036132	0.212326	0.207373	12.087301	12.124754	5.934514	7.968589	3.770021
19	1.743156	0.039516	0.216813	0.177734	10.009308	10.019832	8.290595	11.525789	4.598512
20	1.743156	0.039516	0.216813	0.177734	10.009306	10.019830	8.290594	11.525789	4.598512
22	1.342881	0.030456	0.275675	0.645170	28.681748	28.454762	9.304288	10.84505	9.529707
23	2.394112	0.052429	0.258989	0.524441	27.776368	27.776084	8.772487	11.757885	6.742939
40	1.294653	0.031035	0.072278	0.769060	9.2498850	9.1936510	54.803872	60.375929	5.116731
45	3.343356	0.077355	0.880538	1.389527	16.957517	16.943789	15.190825	19.469721	11.02105
46	3.526740	0.075238	0.524650	1.158338	47.738687	47.493252	10.554401	10.582473	15.844668
47	2.394112	0.052429	0.258989	0.524441	27.776366	27.776082	8.77249	11.757894	6.742938
48	1.335271	0.031420	0.363151	0.235935	43.775435	43.604746	15.335545	19.969860	12.020323
52	0.413789	0.017477	0.035915	0.034995	14.635503	14.619764	3.114262	3.889988	1.069105
53	1.743156	0.039516	0.216813	0.177734	10.009310	10.019834	8.290596	11.52579	4.598513
55	1.342881	0.030456	0.275675	0.645170	28.681752	28.454766	9.304288	10.845048	9.529708
56	2.394112	0.052429	0.258989	0.524441	27.776369	27.776085	8.772485	11.757881	6.742939
57	1.347416	0.036132	0.212326	0.207373	12.087296	12.124749	5.934514	7.968589	3.770021

rate of the central Altyn Tagh Fault vary from 2 to 40 mm yr^{-1} [34,35]. Based on radiocarbon and ^{10}Be–^{26}Al cosmic ray exposure dating of geomorphic markers left-laterally displaced by the Altyn Tagh Fault, Meriaux et al. [32] estimated an average slip rate along the fault to be 26.9 (±6.9) mm yr^{-1}. But the geodetic and satellite radar interferometry observations give much lower slip rates than those estimated for the longer time interval. GPS measurements indeed give a slip rate along the fault at about 10 mm yr^{-1} [27–29], and surface displacement measurements using InSAR provide estimates of slip rates about 5 (±5) mm yr^{-1} [26].

Based on offsets up to a thousand km of geologic markers along the Karakorum fault and the age of the motion (about 30 Myr), the slip rate along the fault is estimated to be about 30 mm yr^{-1} [9]. However, based on other geological observations, lower slip rates of 4 to 8 mm yr^{-1} have been reported [36,37]. ^{10}Be surface exposure dating of offset moraines yields a long-term (up to 0.14 Myr) slip rate of 10.7 (±0.7) mm yr^{-1} [33]. On the other hand, geodetic measurements made over ten years suggest rates of 3 (±5) mm yr^{-1} [31] and 11 (±4) mm yr^{-1} [30]; the estimates based on InSAR measurements give only 1(±3) mm yr^{-1} [26].

Such differences in the slip-rate determinations on the major faults in the Tibetan plateau (apart from possible systematic errors in the GPS or geological estimates) could be explained by variations in (i) the rheological properties of the fault plane zones and/or the lower crust and (ii) movements of the lower crust. The rheological properties of the fault plane zones may vary with time. A change in stress and/or in fluid pressure on a cracked material of the fault zones will result in a distortion of the cracks, which will alter the effective elastic parameters of the faults zone [65,66]. Presence of water can also greatly reduce the viscosity of the fault zones [67], hence increasing fault slip rates. Anisotropy models [68,69] suggest lateral lower crustal flow, which can act as a driving force for rigid upper crustal blocks. Results of the numerical modeling show that relatively small changes in the lower crustal flow can significantly change slip rates and seismicity patterns [see also 42,70].

Based on the combined analysis of earthquake clustering, FM plots, mechanisms of earthquakes, block displacement, and fault slip rates for all sets of numerical experiments, we can mark experiments 4.3, 4.4, and 4.5 as most consistent with the observations (we refer to the experiments as 'preferred'). The patterns of seismic events in the preferred experiments reveal features of observed seismicity (compare Fig. 6a and d–f). Focal mechanisms of observed and preferred synthetic events are in a good agreement (Table 8). The average slip rates on segments S23, S45–S47 (corresponding to the Karakorum fault segments) and

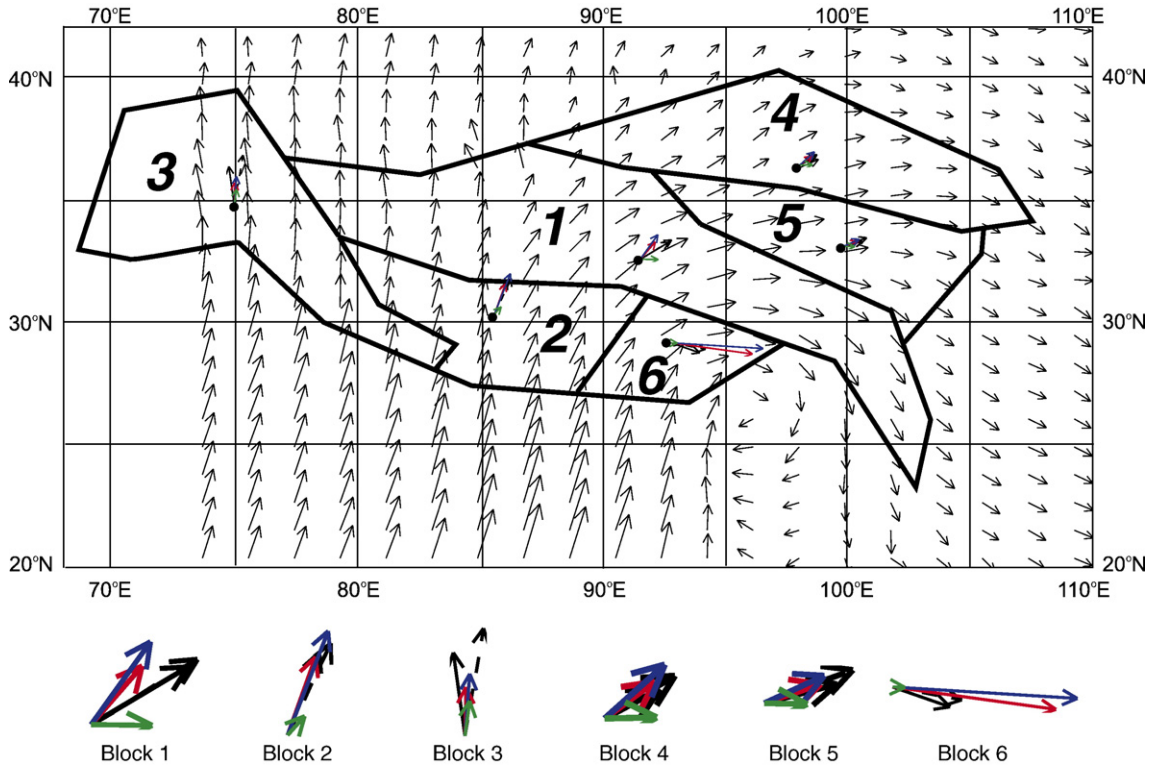

Fig. 9. GPS measurements of the horizontal movements in the region (unpublished compilation of existing data by A. Yin and Z.-K. Shen) and movements of blocks 1 to 6 predicted by the model at the geometrical centers of the blocks. Upper panel: Arrows show the rates of observed horizontal movements. Lower panel: Black solid (and dashed) arrows present interpolated rates (and uncertainty) of observed horizontal movement at the geometrical centers of the blocks. Color solid arrows present modeled rates of horizontal movements in experiment 4.3 (red), experiment 4.4 (blue), and experiment 4.5 (green).

on segments S12–S14 (corresponding to the Altyn Tagh fault segments) vary from 8 to 20 mm yr^{-1} and are consistent with the magnitudes of slip rates on the faults determined by GPS measurements. The discrepancy between the observed slip rates and that obtained on segments S2 and S40 in experiments 4.3 and 4.4 can be associated with the complex movements in the East Lhasa Himalayas and the surrounding area as compared to the motion of block 6 in the model (Fig. 9). Nevertheless, the rotation of model blocks (in the preferred experiments) shows a good agreement with the directions of the regional movement determined also by GPS (Fig. 9).

6. Conclusion

The BAFD model provides a tool for studying both deformations (e.g. stress, strain, slip and slip rates) and seismicity (e.g., clustering of earthquakes, relationships between frequency and magnitude of the events, interaction between earthquakes). Moreover, numerical modeling of crustal/lithospheric dynamics is useful in earthquake prediction studies [38,39]. We have developed the BAFD model of the Tibet plateau and Himalayans, which incorporates the major regional geological structural elements, and performed numerical experiments addressed to a better understanding of the dynamics of the crustal seismicity and fault slip rates in the region.

The present BAFD model of the Tibet-Himalayan region is rather simple, and further development are needed and foreseen, namely: a modification of the block structure and an increase of the thickness of the crustal blocks in South Tibet and Himalayans to obtain events with a larger magnitude; and an introduction of a non-linear rheology of the fault zones to see how it influences seismicity and fault slip rates.

Nevertheless the results of the present numerical modeling lead us to the following conclusions.

1. The contemporary crustal dynamics and seismicity pattern in the region are indeed determined by the

north–northeastern motion of India relative to Eurasia and the movement of the lower crust overlain by the upper crustal rigid blocks.
2. Variations in rheological properties of the fault zones and/or of the lower crust as well as in the motion of the lower crust influence the displacement rates of the crustal blocks and hence the slip rates at the faults separating the blocks. This may explain the discrepancies in the estimates of slip rates at major faults in the region based on different techniques.
3. Clustering of earthquakes can be considered as a consequence of the dynamics of the crustal blocks and faults in the region. The number and maximum magnitude of synthetic earthquakes change with the variations in the movements of the crustal blocks and in the rheological properties of the lower crust and the fault zones.

Acknowledgements

We are thankful to An Jin, John Reinecker, and Peter Shebalin for fruitful discussion on the regional slip rates and earthquake modeling. An Jin and Zheng-Kang Shen provided us with GPS data in the region. We are very grateful to Ross Stein, an anonymous reviewer and Claude Jaupart (as an Editor), who provided careful reviews that significantly improved an initial version of the manuscript. Figs. 1 and 6 have been produced by using Seismic-Eruption software by A. Jones. The study was supported by a special grant of the French Ministry of Research.

References

[1] M. Barazangi, J. Ni, Velocities and propagation characteristics of Pn and Sn beneath the Himalayan arc and Tibetan plateau: possible evidence for underthrusting of Indian continental lithosphere beneath Tibet, Geology 10 (1982) 179–185.
[2] A. Him, et al., Lhasa block and bordering sutures — a continuation of a 500-km Moho traverse through, Nature 307 (1984) 25–27.
[3] X. Le Pichon, M. Fournier, L. Jolivet, Kinematics, topography, shortening, and extrusion in the India–Eurasia collision, Tectonics 11 (6) (1992) 1085–1098.
[4] K.D. Nelson, et al., Partially molten middle crust beneath southern Tibet: synthesis of project INDEPTH results, Science 274 (1996) 1684–1688.
[5] P. Molnar, P. Tapponnier, Active tectonics of Tibet, J. Geophys. Res. 83 (1978) 5361–5375.
[6] P. Tapponnier, et al., Mesozoic ophiolites, sutures, and large-scale tectonic movements in Afghanistan, Earth Planet. Sci. Lett. 52 (1981) 355–371.
[7] R. Armijo, P. Tapponnier, J.L. Mercier, T.-L. Han, Quaternary extension in Southern Tibet: field observations and tectonic implications, J. Geophys. Res. 91 (B14) (1986) 13803–13872.
[8] R. Armijo, P. Tapponnier, H. Tonglin, Late Cenozoic right lateral strike-slip faulting in southern Tibet, J. Geophys. Res. 94 (B3) (1989) 2787–2838.
[9] G. Peltzer, P. Tapponnier, Formation and evolution of strike slip faults, rifts, and basins during the India–Asia collision: an experimental approach, J. Geophys. Res. 93 (B12) (1988) 15,085–15,117.
[10] J.P. Avouac, P. Tapponnier, Kinematic model of active deformation in central-Asia, Geophys. Res. Lett. 20 (10) (1993) 895–898.
[11] E. Fielding, B.L. Isacks, M. Barazangi, C. Duncan, How flat is Tibet? Geology 22 (1994) 163–167.
[12] P. England, P. Molnar, Active deformation of Asia: from kinematics to dynamics, Science 278 (1997) 647–650.
[13] P. England, P. Molnar, The field of crustal velocity in Asia calculated from Quaternary rates of slip on faults, Geophys. J. Int. 130 (1997) 551–582.
[14] G. Houseman, P. England, A lithospheric-thickening model for the Indo-Asian collision, in: A. Yin, T.M. Harrison (Eds.), The Tectonic Evolution of Asia, Cambridge Univ. Press, New York, 1996, pp. 3–17.
[15] P. Bird, Lateral extrusion of lower crust from under high topography, in the isostatic limit, J. Geophys. Res. 96 (1991) 10,275–10,286.
[16] L.H. Royden, B.C. Burchfiel, R.W. King, Z. Chen, F. Shen, Y. Liu, Surface deformation and lower crustal flow in eastern Tibet, Science 276 (1997) 788–790.
[17] M.K. Clark, L.H. Royden, Topographic ooze: building the eastern margin of Tibet by lower crustal flow, Geology 28 (2000) 703–706.
[18] C. Beaumont, R.A. Jamieson, M.H. Nguyen, B. Lee, Himalayan tectonics explained by extrusion of a low-viscosity channel coupled to focused surface denudation, Nature 414 (2001) 738–742.
[19] P. Tapponnier, G. Peltzer, A.Y. Le Dain, R. Armijo, P. Cobbold, Propagating extrusion tectonics in Asia: new insights from simple experiments with plasticine, Geology 10 (1982) 611–616.
[20] P. Tapponnier, X. Zhiqin, B. Meyer, F. Roger, N. Arnaud, G. Wittlinger, Y. Jingsui, Asymmetric, stepwise rise and growth of the Tibet Plateau, Science 294 (2001) 1671–1677.
[21] G. Peltzer, F. Saucier, Present-day kinematics of Asia derived from geologic fault rates, J. Geophys. Res. 101 (1996) 27,943–27,956.
[22] S. McClusky, et al., Global positioning system constraints on plate kinematics and dynamics in the eastern Mediterranean and Caucasus, J. Geophys. Res. 105 (2000) 5695–5719.
[23] J. Vergnes, et al., Seismic evidence for stepwise thickening of the crust across the NE Tibetan Plateau, Earth Planet. Sci. Lett. 203 (2002) 25–33.
[24] G. Wittlinger, J. Vergne, P. Tapponnier, V. Farra, G. Poupinet, M. Jiang, H. Su, G. Herquel, A. Paul, Teleseismic imaging of subducting lithosphere and Moho offsets beneath western Tibet, Earth Planet Sci. Lett. 221 (2004) 117–130.
[25] G. Wittlinger, et al., Tomographic evidence for localized lithospheric shear along the Altyn Tagh Fault, Science 282 (1998) 74–76.
[26] T.J. Wright, B. Parsons, P.C. England, E.J. Fielding, InSAR observations of low slip rates on the major faults of western Tibet, Science 304 (2004) 236–239.
[27] R. Bendick, R. Bilham, J. Freymueller, K. Larson, G. Yin, Geodetic evidence for a slip rate in the Altyn Tagh fault system, Nature 404 (2000) 69–72.
[28] Z. Chen, B.C. Burchfiel, Y. Liu, R.W. King, L.H. Royden, W. Tang, E. Wang, J. Zhao, W. Zhang, GSA measurements from eastern Tibet and their implications for India/Eurasia intracontinental deformation, J. Geophys. Res. 105 (2000) 16215–16227.

[29] Z.K. Shen, C. Zhao, A. Yin, Y. Lin, D.D. Jackson, P. Fang, D. Dong, Contemporary crustal deformation in East Asia constrained by Global Positioning System measurements, J. Geophys. Res. 105 (2000) 5721–5734.
[30] P. Banerjee, R. Bürgmann, Convergence across the northwest Himalayas from GPS measurements, Geophys. Res. Lett. 29 (13) (2002), doi:10.1029/2002GL 015184.
[31] J. Jade, et al., GPS measurements from the Ladakh Himalayas, India: preliminary tests of plate-like or continuous deformation in Tibet, Geol. Soc. Amer. Bull. 116 (2004) 1385–1391.
[32] A.-S. Meriaux, F.J. Ryerson, P. Tapponnier, J. Van der Woerd, R.C. Finkel, X. Xu, Z. Xu, M.W. Caffee, Rapid slip along the central Altyn Tagh Fault: morphochronologic evidence from Cherchen He and Sulamu Tagh, J. Geophys. Res. 109 (2004), doi:10.1029/2003JB002558.
[33] M.L. Chevalier, F.J. Ryerson, P. Tapponnier, R.C. Finkel, J. Van Der Woerd, L. Haibing, L. Qing, Slip-rape measurements on the Karakorum fault may imply secular variations in fault motion, Science 307 (2005) 411–414.
[34] G. Peltzer, P. Tapponnier, R. Armijo, Magnitude of Late Quaternary left-lateral displacements along the north edge of Tibet, Science 246 (1989) 1285–1289.
[35] S. Ge, G. Shen, R. Wei, G. Ding, Y. Wang, Active Altyn Fault Zone, Monograph, State Seismol. Bur. of China, Beijing, 1992, 319 pp.
[36] M.P. Searle, R.F. Weinberg, W.J. Dunlap, Transpressional tectonics along the Karakoram fault zone, northern Ladakh: constraints on Tibetan extrusion, in: R.E. Holdsworth, R.A. Strachan, J.F. Dewey (Eds.), Continental Transpressional and Transtensional Tectonics, Special Publication, vol. 135, Geological Society, London, 1998, pp. 307–325.
[37] E.T. Brown, R. Bendick, D.L. Bourles, V. Gaur, P. Molnar, G.M. Raisbeck, F. Yiou, Slip rates of the Karakorum fault, Ladakh, India, determined using cosmic ray exposure dating of debris flows and moraines, J. Geophys. Res. 107 (B9) (2002), doi:10.1029/2000JB000100.
[38] A.M. Gabrielov, T.A. Levshina, I.M. Rotwain, Block model of earthquake sequence, Phys. Earth Planet. Inter. 61 (1990) 18–28.
[39] A. Soloviev, A. Ismail-Zadeh, Models of dynamics of block-and-fault systems, in: V. Keilis-Borok, A. Soloviev (Eds.), Nonlinear Dynamics of the Lithosphere and Earthquake Prediction, Springer-Verlag, Berlin-Heidelberg, 2003, pp. 71–139.
[40] G.F. Panza, A.A. Soloviev, I.A. Vorobieva, Numerical modeling of block-structure dynamics: application to the Vrancea region, Pure Appl. Geophys. 149 (1997) 313–336.
[41] A.A. Soloviev, I.A. Vorobieva, G.F. Panza, Modeling of block–structure dynamics: parametric study for Vrancea, Pure Appl. Geophys. 156 (1999) 395–420.
[42] A.T. Ismail-Zadeh, V.I. Keilis-Borok, A.A. Soloviev, Numerical modeling of earthquake flow in the south-eastern Carpathians (Vrancea): effect of a sinking slab, Phys. Earth Planet. Inter. 111 (1999) 267–274.
[43] R.S. Stein, The role of stress transfer in earthquake occurrence, Nature 402 (1999) 605–609.
[44] T. Utsu, A. Seki, A relation between the area of aftershock region and the energy of main shock, J. Seismol. Soc. Jpn. 7 (1954) 233–240.
[45] A. Replumaz, P. Tapponnier, Reconstruction of the deformed collision zone between Indian and Asia by backward motion of lithospheric blocks, J. Geophys. Res. 108 (2003), doi:10.1029/2001JB000661.
[46] P. Tapponnier, P. Molnar, Active faulting and tectonics in China, J. Geophys. Res. 82 (1977) 2905–2930.
[47] P. Tapponnier, P. Molnar, Active faulting and Cenozoic tectonics of the Tien Shan, Mongolie, and Baikal regions, J. Geophys. Res. 84 (1979) 3425–3459.
[48] A.Y. Le Dain, P. Tapponnier, P. Molnar, Active faults and tectonics of Burma and surrounding regions, J. Geophys. Res. 89 (1984) 453–472.
[49] Y. Gaudemer, P. Tapponnier, B. Meyer, G. Peltzer, G. Shunmin, C. Zhitai, D. Huagung, I. Cifuentes, Partitioning of crustal slip between linked, active faults in the eastern Qilian Shan, and evidence for a major seismic gap, the "Tianzhu gap", on the western Haiyuan Fault, Gansu (China), Geophys. J. Int. 120 (1995) 599–645.
[50] J. Van Der Woerd, F.J. Ryerson, P. Tapponnier, Y. Gaudemer, R. Finkel, A.S. Meriaux, M. Caffee, Z. Guoguang, H. Qunlu, Holocene left-slip rate determined by cosmogenic surface dating on the Xidatan segment of the Kunlun fault (Qinghai, China), Geology 26 (1998) 695–698.
[51] J. Van Der Woerd, F.J. Ryerson, P. Tapponnier, A.S. Meriaux, Y. Gaudemer, B. Meyer, R. Finkel, M. Caffee, G. Zhao, Z.Q. Xu, Uniform slip-rate along the Kunlun Fault: implications for seismic behaviour and large-scale tectonics, Geophys. Res. Lett. 27 (2000) 2353–2356.
[52] C. Lasserre, P.H. Morel, Y. Gaudemer, P. Tapponnier, F.J. Ryerson, G. King, F. Metivier, M. Kasser, M. Kashgarian, L. Baichi, L. Taiya, Postglacial left slip rate and past occurrence of M>=8 earthquakes on the western Haiyuan fault, Gansu, China, J. Geophys. Res. 104 (1999) 17,633–17,651.
[53] A. Yin, Mode of Cenozoic east–west extension in Tibet suggesting a common origin of rifts in Asia during the Indo-Asian collision, J. Geophys. Res. 105 (2000) 21,745–21,759.
[54] B. Meyer, P. Tapponnier, L. Bourjot, F. Metivier, Y. Gaudemer, G. Peltzer, G. Shunmin, C. Zhitai, Mechanisms of active crustal thickening in Gansu–Qinghai, and oblique, strike-slip controlled, northeastward growth of the Tibet Plateau, Geophys. J. Int. 133 (1998) 1–47.
[55] R. McCaffrey, J. Nabelek, Role of oblique convergence in the active deformation of the Himalayas and southern Tibet plateau, Geology 26 (1998) 691–694.
[56] M.L. Hauck, K.D. Nelson, L.D. Brown, W. Zhao, A.R. Ross, Crustal structure of the Himalayan orogen at ~90° east longitude from Project INDEPTH deep reflection profiles, Tectonics 17 (1998) 481–500.
[57] D. Alsdorf, L. Brown, K.D. Nelson, Y. Makovsky, S. Klemperer, W. Zhao, Crustal deformation of the Lhasa terrane, Tibet plateau, from Project INDEPTH deep seismic reflection profiles, Tectonics 17 (1998) 501–519.
[58] J.G. Mazek, B.L. Isacks, E.J. Fielding, Rift flank uplift in Tibet: evidences for a viscous lower crust, Tectonics 13 (1994) 659–667.
[59] R. Bilham, K. Larson, J. Freymueller, Project Idylhim members, GPS measurements of present-day convergence across the Nepal Himalayas, Nature 386 (1997) 61–64.
[60] K.Y. Abdrakhmatov, et al., Relatively recent construction of the Tien Shan inferred from GPS measurements of present day crustal deformation rate, Nature 384 (1996) 450–453.
[61] S. Wang, et al., Present-day crustal deformation in China constrained by Global Positioning System measurements, Science 294 (2001) 574–577.
[62] B.C. Burchfiel, New technology; new geological challenges, GSA Today 14 (2) (2004) 4–10.
[63] C.J. Allegre, J.-L. Le Mouël, H.D. Chau, C. Narteau, Scaling organization of fracture tectonics (SOFT) and earthquake mechanism, Phys. Earth Planet. Inter. 92 (1995) 215–233.

[64] D.L. Wells, K.J. Coppersmith, New empirical relationships among magnitude, rupture length, rupture width, rupture area, and surface displacement, Bull. Seismol. Soc. Am. 84 (4) (1994) 974–1002.
[65] J.A. Hudson, The effect of fluid pressure on wave speeds in a cracked solid, Geophys. J. Int. 143 (2000) 302–310.
[66] S.R. Tod, The effects of stress and fluid pressure on the anisotropy of interconnected cracks, Geophys. J. Int. 149 (2002) 149–156.
[67] P.N. Chopra, M.S. Paterson, The role of water in the deformation of dunite, J. Geophys. Res. 89 (1984) 7861–7876.
[68] N.M. Shapiro, M.H. Ritzwoller, P. Molnar, V. Levin, Thinning and flow of Tibetan crust constrained by seismic anisotropy, Science 305 (2004) 233–236.
[69] A.A. Ozacar, G. Zandt, Crustal seismic anisotropy in central Tibet: implications for deformational style and flow in the crust, Geophys. Res. Lett. 31 (2004), doi:10.1029/2004GL021096.
[70] F. Press, C. Allen, Pattern of seismic release in the southern California region, J. Geophys. Res. 100 (1995) 6421–6430.